Dichroism in the electron-impact ionization of excited and oriented sodium atoms

J. Lower,[1] A. Elliott,[1] E. Weigold,[1] S. Mazevet,[1,*] and J. Berakdar[2]

[1]*Atomic and Molecular Physics Laboratories, Institute of Advance Studies, Research School of Physical Sciences and Engineering, Australian National University, Canberra ACT 0200, Australia*

[2]*Max-Planck Institute for Microstructure Physics, Weinberg 2, 06120 Halle, Germany*

Measurements are reported for kinematically complete electron-impact ionization collisions with oriented $3P$ sodium atoms excited from the ground state by right- and left-hand circularly polarized light. The measurements reveal a strong dependence of the ionization cross section on the helicity inversion of the exciting photon. This dichroic effect and the magnetic state resolved cross sections are described using the distorted-wave Born approximation and the dynamically screened Coulomb wave method. Within the context of these methods we investigate the role of different short- and long-range interactions involved in the process. For moderate values of incident energy we conclude that the shape and magnitude of the dichroism is predominantly determined by the Coulomb interactions of the outgoing electrons with the residual ion. For slow escaping electrons the dichroism is also influenced by the interelectronic correlations.

I. INTRODUCTION

The need for a detailed understanding of the process of ionization by electron impact for various fields of physics, such as atmospheric physics, plasma physics, and gas discharge physics, has led to extensive studies both experimental and theoretical of this particular process. The most complete information on the electron-impact ionization process is obtained from so-called $(e,2e)$ experiments, where both the scattered and the ejected electrons from the target are detected in coincidence and their momenta are resolved. This kind of measurement has proved indispensible when addressing the details of collision dynamics. Moreover, the $(e,2e)$ technique can be employed for the spectroscopy of electronic structure of atoms, molecules, and solids [1,2]. These different aspects of the $(e,2e)$ reaction can be highlighted by judicious choice of the kinematic arrangement.

In recent years, a new generation of $(e,2e)$ experiments has emerged that uses polarized electron beams and/or atomic beams in which the constituent atoms are aligned and/or oriented. The first $(e,2e)$ experiment of this type used a polarized electron beam to ionize lithium atoms prepared in a particular quantum state by use of inhomogeneous magnetic fields, and was primarily concerned with the study of the exchange process [3]. These experiments were followed by experimental arrangements using a polarized electron beam at relativistic energy for the inner-shell ionization of various atomic targets such as silver [4] and at intermediate energy for the outer-shell ionization of xenon, where the fine structure energy splitting of the residual ion can be resolved experimentally [5,6]. High-energy experiments on the inner shells of heavy target atoms were primarily concerned with the study of the influence of relativistic interactions during the ionization process [7]. In the xenon experiments, experimental verification of the so-called fine structure effect in

electron-impact ionization [8–10] was established and comparison of the results with theory revealed detailed information on the influence of the short-range interactions between the two outgoing electrons and the residual ion [6,9].

In this paper we focus on the electron-impact ionization of sodium atoms laser pumped into a well defined angular momentum magnetic substate. In this situation the $(e,2e)$ cross section reveals a dependence on the inversion of the helicity of the exciting photon [11,12]. This dichroic effect results from the transfer of the initial-state orientation to the outgoing correlated electron pair and hence has been termed *orientational dichroism*. Experimental evidence for the existence of this effect has been provided recently by Dorn *et al.* [12]. Here, we present further experimental and theoretical results and investigate in more detail the underlying physical processes.

Experimentally, the sodium atoms are prepared in the $(3\,^2P_{3/2},\ F=3,\ m_F=\pm 3)$ hyperfine states and ionized using an initially unpolarized electron beam. Initial theoretical and experimental studies [11–14] indicate a strong dependence of the cross section on the direction of the initial-state atomic orientation. This dependence of the cross sections is most easily analyzed within the theoretical framework of the first Born approximation (FBA), i.e., when we assume that the ejected electron moves in the field of the residual ion whereas the scattered one is free. In this case the geometrical properties of the orientational dichroism are given by the triple product of the quantization axis of the atom, the momentum transfer direction, and the vector momentum of the ejected electron [11,12]. According to the FBA model, the origin of the dichroism lies in the interaction of the slow electron with the residual ion; the dichroism vanishes when this interaction is neglected [15]. Furthermore, the FBA predicts that the cross sections for the electron-pair emission from left- or right-hand circularly laser-pumped Na atoms are related to each other via reflection symmetry about the direction of momentum transfer [15].

Recent experimental measurements [12–14] reveal a considerable break of this symmetry property which indicates a
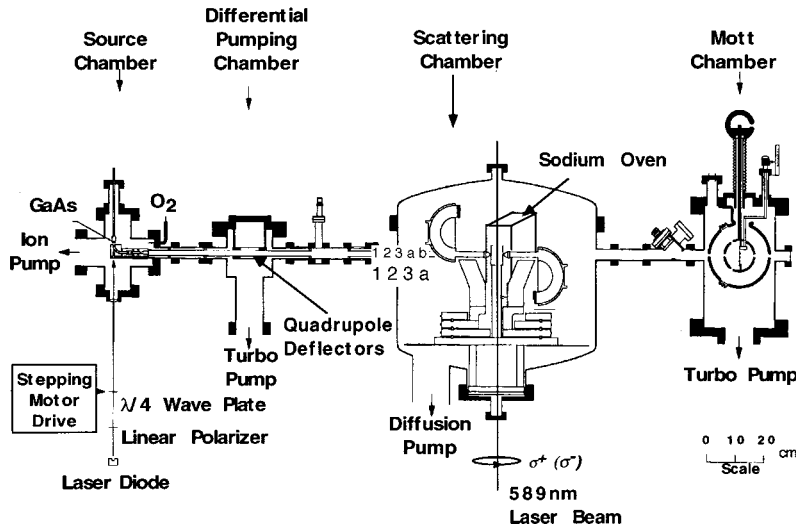
FIG. 1. Schematic of the electron source and coincidence spectrometer.

dynamical transfer of the initial atomic orientation to the two outgoing electrons through mechanisms beyond those simulated by the FBA. On the grounds of an approximate model for the correlated many-body dynamics, it was proposed that this symmetry breaking has its origin in the final-state electron correlation [12–14]. As the theoretical interpretation is subject to the approximation adopted for the treatment of the reaction dynamics, we contrast in this work the predictions of various approximative scattering models with experimental findings. We first employ the distorted-wave Born approximation [16,17], which is particularly convenient for isolating the influence of the various interactions between the continuum and target electrons, and then the more refined dynamically screened Coulomb wave method [18] to quantify the influence of the final-state electron correlations.

The paper is organized as follows. In the next section we give an outline of the experimental procedure. We then address the theoretical framework necessary to describe this particular experimental situation. In the fourth section, we outline the main features of the scattering methods that are particularly relevant to the present study. In the last section, we investigate the influence of the short- and long-range interactions and the electron-electron correlations on the calculated cross sections and compare them with our experimental data.

II. EXPERIMENTAL ARRANGEMENT

A. Apparatus

In Fig. 1 the apparatus is shown schematically. It can be divided into three components comprising the source and differential pumping chambers in which generation and transport of the primary electron beam is achieved, the scattering chamber in which the atom beam is formed, the intersection of the laser, electron, and atom beams occurs, and the $(e,2e)$ ionization processes are measured, and finally the Mott chamber in which the degree of the incident electron beam polarization can be determined. The Mott chamber was not utilized in the present measurements and will not be described here. Each of the other stages is discussed in sequence below.

The first stage of the apparatus consists of two ultrahigh-vacuum (UHV) chambers connected in series with one another. In the first of these chambers, the so-called source chamber, electrons are produced by irradiation of a negative-affinity p-doped GaAs crystal surface by laser light. The details of the crystal composition, cleaning, and coating procedure have been described previously [19] and will not be repeated here. This first chamber is pumped by a 30 l/s ion pump which maintains a background pressure in the 10^{-11} torr range. The combination of an UHV environment to minimize contamination of the GaAs photocathode and a continuous deposition of cesium onto the photocathode surface enables stable emission currents to be maintained over a period of many months. Linearly polarized light from a GaAlAs diode laser of around 810 nm wavelength is used to generate the photoelectrons. The laser beam is first passed through a focusing lens and a 1/4 wave plate to produce circularly polarized radiation before impinging upon the crystal surface. Photon fluxes of a few milliwatts are sufficient to produce microamperes of current.

Using extraction by an electrostatic field, the photoelectrons are formed into an electron beam. For excitation by circularly polarized light incident perpendicular to the surface, the beam is polarized either parallel or antiparallel to the direction of electron motion, depending upon the helicity of the radiation used in the photoexcitation process. For GaAs the polarization of the electron beam is theoretically limited to a maximum value of 50% due to the selection rules governing the transitions excited in the photoemission process. We obtain a polarization value routinely of around 24–30 % in our system, the difference between this value and the theoretical maximum being attributed to depolarizing effects acting on the photoelectrons as they are transported from within the bulk to the surface of the photocathode [20]. Inversion of the electron beam polarization can be achieved by reversing the helicity of the laser light through rotation of the 1/4 wave plate by 90°. As an applied electrostatic field will act on the trajectory of an electron beam but not on its angular momentum, the initially longitudinally polarized electron beam is converted to one of transverse polarization by deflecting it through a 90° electrostatic deflector. This

action is desirable as for many of our experiments a transversely polarized electron beam is required. However, for the present measurements unpolarized electrons were used. This was achieved by rotating the quarter wave plate to an angular position producing linearly polarized radiation. After extraction of the photoelectrons and their transmission through the 90° deflector, a system of electrostatic cylindrical tube lenses and deflectors is used to focus and accelerate the electron beam to 1000 eV and steer it through the 3-mm-diameter aperture separating the source chamber from the differential pumping chamber.

The purpose of the differential pumping chamber is to provide a differential pumping stage between the source chamber and the non-UHV scattering chamber to minimize contamination of the GaAs photocathode. The differential pumping chamber is pumped by a 180 l/s turbo molecular pump and maintains a base pressure of around 5×10^{-10} torr. It is separated from the scattering chamber by a second 3 mm aperture at its exit. Within the differential pumping chamber are two sets of quadrupole deflectors to steer the 1000 eV electron beam through the exit aperture into the main scattering chamber, compensating for perturbations to the beam trajectory from spurious magnetic fields and surface charging effects within the electron optics. Transporting the beam from the source to the scattering chamber at high energy has two advantages. First, it renders the beam less sensitive to the effects of deflection and defocusing by stray magnetic fields. Secondly, the narrower beam profile achieved by using higher beam energies enables the use of smaller apertures at the entrance and exit of the differential pumping chamber, increasing the pressure gradient that can be maintained between the source and scattering chambers.

In the scattering chamber the electron passes through a further series of cylindrical tube lenses which are used to both collimate and decelerate the beam to the required impact energy. A target beam of sodium atoms is produced by effusion of sodium vapor through a 1 mm aperture in the output stage of a recirculating metal vapor oven described in detail below. The interaction region lies in the scattering plane defined by the momentum vectors of the sodium beam and the incident and detected scattered electrons, the latter three quantities constrained to share a common plane under the coplanar reaction kinematics employed for the present work. The intersection of the sodium and electron beams defines the interaction region from which ($e,2e$) events are measured. The interaction region also lies on the axis of rotation of three rotatable turntables. On one of the turntables the sodium oven is mounted. On each of the remaining two turntables an electron spectrometer is mounted.

Each of the two electron spectrometers comprises a 180° hemispherical electrostatic electron analyzer preceded by a five-element cylindrical lens system. The combination of the energy selecting analyzer and the angle resolving lens system defines the momentum and energy of measured scattered electrons. The lens system is similar in design to that described in Ref. [21] and comprises two three-element zoom lenses in series sharing a common central lens, allowing independent control over energy and angular resolution to be achieved. Position-sensitive detectors are mounted at the exit
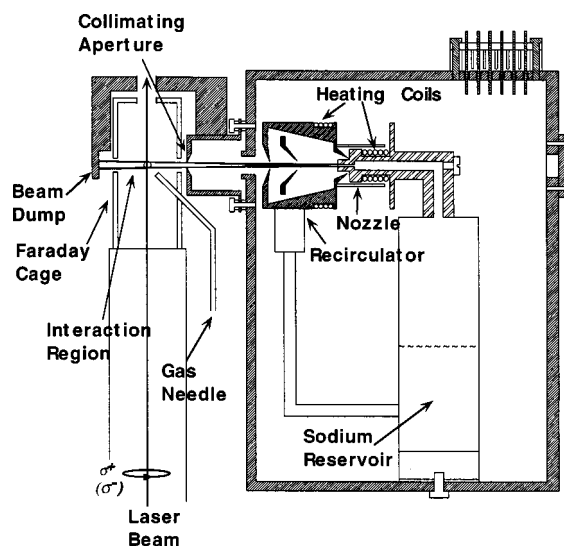

FIG. 2. Outline of recirculating sodium oven and interaction region. The copper walls of the oven surround are water cooled. The exit aperture and beam dump are cooled by liquid nitrogen.

plane of each analyzer, behind a slit in the radial direction, enabling simultaneous measurement of scattered electrons over a 6 eV energy band with an energy resolution of around 200 meV and at an angular resolution of around 2° full width at half maximum.

The sodium oven, constructed of stainless steel, is shown schematically in Fig. 2 and is similar in design to that described in Ref. [22]. It is comprised of three distinct components, namely, the reservoir, the nozzle, and the recirculator. The reservoir consists of a cylindrical vessel containing sodium around which heating wire is wrapped to provide ohmic heating. Reservoir temperatures of between 400 and 450 °C are necessary to produce the required target densities for our measurements. The temperature of the reservoir and other key components is monitored by use of thermocouples. Vapor leaving the reservoir is formed into a beam of sodium atoms within the nozzle stage, which is terminated by a 1-mm-bore capillary of around 10 mm length. The separately heated nozzle is maintained at a temperature at least 100° higher than that of the reservoir to prevent blockage due to the buildup sodium within its narrow exit capillary. The sodium beam emerging from the nozzle is skimmed through the action of an aperture positioned at the exit of the oven recirculation stage. Atoms not contained within the central cone of the nozzle beam are recondensed to the liquid phase upon impact with the recirculator walls, which are maintained at a temperature of between 150 and 200 °C, and subsequently returned to the sodium reservoir. The inclusion of the recirculation stage extends the operating lifetime between sodium refills and, by maintaining the collimating aperture surrounds at a temperature above that required for the formation of solid sodium, circumvents the problems of the closing over of cold collimation apertures with time.

The whole oven assembly is enclosed within a water cooled rectangular copper box whose purpose is twofold. First, it provides a heat sink for radiation emitted by the oven (around 150 W) and, secondly, it offers additional protection
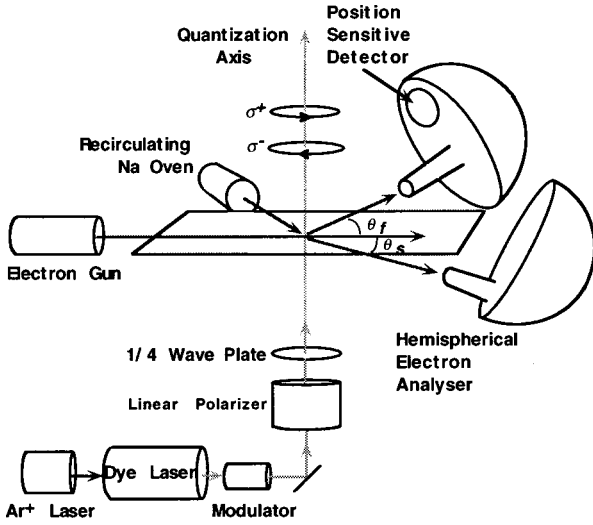
FIG. 3. Schematic of the experimental arrangement showing the coplanar arrangement of the incident and outgoing electron and sodium beams intersecting at the collision region with the perpendicular laser beam.

for delicate vacuum components from residual background sodium vapor or accidental spills of liquid sodium under vacuum. The box is kept compact in design by incorporating V-shaped channels through each of its 8-mm-thick sidewalls through which cooling water is passed. The compact nature of the design maximizes the angular range through which the spectrometers can rotate within the scattering plane.

Mounted off the box is a final stage liquid nitrogen cooled collimating aperture and sodium beam dump to provide further collimation of the beam and additional protection against contamination of the vacuum environment by gaseous sodium. Both are thermally isolated from the box by ceramic insulators and cooled by means of a flexible copper braid connected to a cold finger protruding through the wall of the scattering chamber.

B. Laser preparation of the target

Intersecting the scattering plane at right angles and completely encompassing the interaction region is a frequency modulated 589 nm laser beam used to excite and orientate the sodium target atoms by preparing them in a specific hyperfine magnetic substate. The initially linearly polarized laser light is converted to circularly polarized radiation by transmission through a quarter wave plate, the rotation of which by 90° reverses the helicity of the radiation field and thus the orientation of the excited-state atoms. The laser beam preparation is shown in Fig. 3, which shows schematically the experimental arrangement.

In order to reach a high fraction of laser excited atoms in the interaction region, the laser excitation is performed by means of two frequencies produced by frequency modulation of a single-mode dye laser beam. Frequency modulation is achieved by passing the laser beam through an electro-optical modulator which is similar in design to that reported in [23]. It consists of a rectangular $LiTaO_3$ crystal embedded within a copper foil resonator. Power is coupled into the

modulator by mutual induction with a single-loop drive coil. The application of a resonator ensures that for modest rf power inputs, a large voltage is built up across adjacent faces of the $LiTaO_3$ crystal. To first order, the refractive index of $LiTaO_3$ varies linearly with strength of the applied field. It follows then from Fourier analysis that for a sinusoidal driving frequency ω_m and for an incident laser beam of frequency ω_0 passing through the crystal, the output field consists of the primary frequency ω_0 and additional sidebands separated by multiples of ω_m. In the present case for sodium the laser beam is modulated at a frequency of 856 MHz, the first two sidebands being separated by 1712 MHz. One sideband is used to pump the transition $3s^{1\,2}S_{1/2}(F=1) \rightarrow 3p^{1\,2}P_{3/2}(F=2)$ and the other the $3s^{1\,2}S_{1/2}(F=2) \rightarrow 3p^{1\,2}P_{3/2}(F=3)$ transition. In this way a relative fraction α of around 40% $3p^{1\,2}P_{3/2}$ excited-state atoms can be routinely achieved [24]. After a few excitation/decay cycles the atoms gather exclusively in the two-level system $3s^{1\,2}S_{1/2}(F=2,m_F=+2), 3p^{1\,2}P_{3/2}(F=3,m_F=+3)$ for pumping by right-hand circularly polarized light, or in the system $3s^{1\,2}S_{1/2}(F=2,m_F=-2), 3p^{1\,2}P_{3/2}(F=3,m_F=-3)$ for pumping by left-hand circularly polarized light. This is confirmed numerically by solving the corresponding rate equations. The degree of orientation of the excited state in the interaction region was estimated to be between 96% and 100% by comparing superelastic scattering data with those of previous authors [22].

C. Experimental procedure

In order to discriminate between ionization events resulting from the removal of $3s$ and $3p$ electrons, respectively, the binding energy ϵ_I of the ejected electron is determined from the energies of both outgoing continuum electrons E_f and E_s and the energy of the incoming electron E_0 from the relation

$$\epsilon_I = E_0 - (E_f + E_s). \qquad (1)$$

For each measured coincidence event the summed energy spectrum of both detected outgoing electrons is stored on a multichannel analyzer yielding a binding-energy spectrum with a binding-energy resolution given by the convolution of the energy spreads of the incoming beam and the apparatus functions of both of the electron analyzers. In the present case, an $(e,2e)$ binding-energy resolution of around 0.9 eV was achieved, more than sufficient to resolve events corresponding to ionization of the ground- and excited-state atoms, which are separated by 2.14 eV in binding energy.

It should be noted, however, that an energy average has been performed at each binding energy over all combinations of values for E_f and E_s within the 6 eV acceptance band of each analyzer that satisfy Eq. (1). This was undertaken to enable the data to be displayed in a compact form and to improve statistics. Thus, although a high value for binding-energy resolution $\Delta \epsilon_I$ of 0.9 eV is achieved, the energy resolution for both slow and fast scattered electrons, ΔE_s and ΔE_f, respectively, is 6 eV for the experimental data presented in this paper.
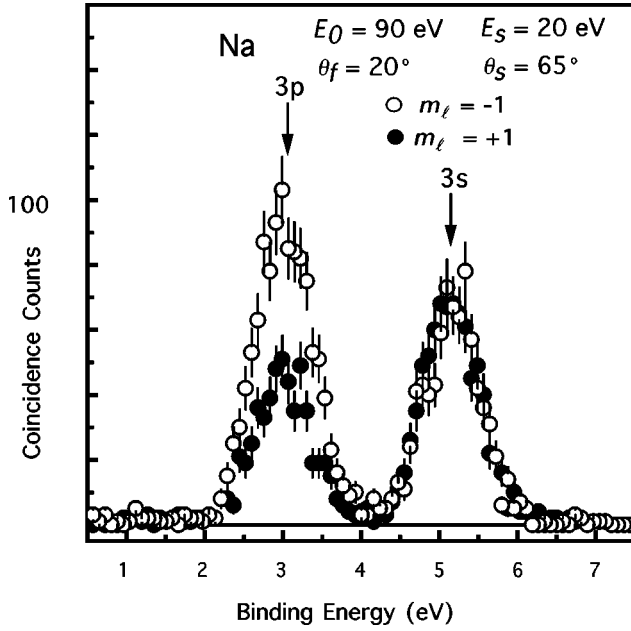
FIG. 4. Sodium ($e,2e$) binding-energy spectra for $E_0=90$ eV, $E_s=20$ eV, $\theta_f=20°$, $\theta_s=65°$, with left- and right-hand circularly polarized optical pumping light, showing the ground-state and excited-state transitions.

For each chosen angular setting of the analyzers, spectra corresponding to positive and negative target orientation are recorded, as well as random coincidence background spectra which are subtracted from the binding-energy spectra in the usual manner [25]. A typical binding-energy spectrum for the two helicities of the incident radiation is shown in Fig. 4.

The experiments consisted of measuring ($e,2e$) binding-energy spectra for a fixed scattering angle θ_f of the fast emitted electron as a function of the scattering angle θ_s for the slow electron and for both positive ($m_F=+3$) and negative ($m_F=-3$) orientations of the excited state. These states consist of maximal projections of the nuclear spin ($I=3/2$), the orbital angular momentum ($l=1$), and the electron spin along the laser beam direction. Neglecting the spin-orbit interaction and for unpolarized incident electrons and no polarization analysis of the final electron, the cross section depends only on the orbital orientation $m_l=\pm1$, and not on the nuclear and electron spin orientations.

Many scans were performed in each experiment to average over the effects of instrumental drifts. Cross normalization of the experimentally derived ground- and excited-state cross sections for each particular kinematic arrangement was achieved in the following manner. For any arbitrary reaction kinematics, the relative fraction α of excited-state atoms is determined by measuring the ($e,2e$) count rates N_{3s}^{on} and N_{3s}^{off}, corresponding to the ionization of ground-state atoms with the pump laser on and off, respectively, through the relation

$$\alpha = 1 - N_{3s}^{\text{on}}/N_{3s}^{\text{off}}. \qquad (2)$$

Having determined the value of α, the ratio of ground- to excited-state cross sections σ_{3s}/σ_{3p}, for a given target ori-

entation ($m_f=+3$ or $m_f=-3$), is derived from the corresponding ($e,2e$) count rates N_{3s}^{on} and N_{3p}^{on} corresponding to ionization of ground- and excited-state atoms, respectively, measured with the pump laser beam on. This is achieved through the relation

$$\sigma_{3s}/\sigma_{3p} = \frac{N_{3s}^{\text{on}}}{N_{3p}^{\text{on}}} \frac{\alpha}{1-\alpha}. \qquad (3)$$

In the present series of measurements, $\alpha=0.45\pm0.04$ for the 151 eV measurements and 0.35 ± 0.05 for the remainder, leading to an error in the relative normalizations of ground- and excited-state data of around 20%.

III. THEORY

A. Formulation

In the most general case of state-selected ($e,2e$) experiments, the atomic beam may be oriented and/or aligned while the incident electron beam may be partially polarized perpendicular to the collision plane defined by the momenta of the incoming and scattered (fast) electrons, respectively denoted as $\mathbf{k}_0$ and $\mathbf{k}_f$. Following the methodology used for the description of state-selected elastic and inelastic scattering experiments [26–28], we use the density matrix formalism to describe such ($e,2e$) experiments and to take into account the information relevant to the initial-state preparation [29]. Within this formulation, the atomic and electron beams are characterized by density operators whose matrix representations reflect the statistical mixture of pure states, each corresponding to the state of one atom or electron present in the beam. The density operator ρ^{in} describing the initial state of the electron-atom system is given by the direct product of the density operators ρ^e and ρ^a that represent, respectively, the electron and atomic beams. This is because the electron and atomic beams are initially prepared far from the interaction region, and as such are assumed to be uncorrelated before the interaction begins [26]. Thus we write

$$\rho^{\text{in}} = \rho^e \times \rho^a. \qquad (4)$$

In the present study, as the initial electron beam is unpolarized, the reduced density matrix of the electron beam is simply the unit matrix, the normalization coefficient reflecting the dimension of the incoming electron spin space,

$$\rho^{\text{in}} = \frac{1}{2} \sum_{\substack{M,M' \\ \nu_0}} |\nu_0,J,M\rangle\langle\nu_0,J,M'| \rho_{M,M'}^J. \qquad (5)$$

The superscript a has been dropped from the density matrix describing the atomic beam. Furthermore, for the pure initial atomic state $|F,M_F\rangle$, we assume that the nonzero nuclear spin of the atom plays no dynamical role in the collision process [30]. The atom is thus described as being prepared in a quantum state $|J,M\rangle$, where J is the total angular momentum of the atom and M its projection along the quantization axis. The effect of the nonzero nuclear spin will appear only

through recoupling coefficients which are dropped in the relation (5). The quantum number ν_0 in Eq. (5) labels the electron spin projections.

The atomic beam is most easily described in the photon frame where the quantization axis $\mathbf{z}^{ph}$ is parallel to the direction of propagation in the case of circularly polarized light and to the direction of the electric field in the case of linearly polarized light [31]. In the photon frame the density matrix of the excited atomic state and the ground state becomes diagonal.

The differential cross section for the ejection of two electrons from an atomic target, initially prepared in a particular quantum state $|JLM\rangle$, upon the impact of an unpolarized electron beam can be expressed as [2,16]

$$\frac{d^5\sigma}{d\Omega_f d\Omega_s dE_s} = \kappa \sum_{\substack{\nu_0 M_i \\ \nu_f \nu_S}} \langle \mathbf{k}_f \nu_f \mathbf{k}_s \nu_s \Phi^{ion}_{J_i L_i M_i} | T | \Phi^{atom}_{JLM} \mathbf{k}_0 \nu_0 \rangle$$
$$\times \langle \Phi^{atom}_{JLM} \mathbf{k}_0 \nu_0 | T^\dagger | \mathbf{k}_f \nu_f \mathbf{k}_s \nu_s \Phi^{ion}_{J_i L_i M_i} \rangle \rho^J_{MM},$$
$$(6)$$

where E_s is the energy of one emitted electron [the energy of the other electron is deduced from Eq. (1)] and $d\Omega_f$ and $d\Omega_s$ are the solid angles associated with $\mathbf{k}_f$ and $\mathbf{k_s}$. Equation (6) assumes no resolution of the spin projections ν_f and ν_s of the two outgoing electrons and no detection of the orientation and/or alignment for the residual ion. The wave function of the atom (residual ion) in a particular quantum state $|JLM\rangle$ ($|J_i L_i M_i\rangle$) is Φ^{atom} (Φ^{ion}) whereas T is the transition operator. The kinematical factor κ is given by

$$\kappa = (2\pi)^4 \frac{k_f k_s}{k_0}.$$
$$(7)$$

As shown in recent articles [11,15], the effect of the initial-state preparation on the collision dynamic is most conveniently seen when state multipoles ρ_{KQ} are used rather than density matrices. The state multipoles ρ_{KQ} are related to the density matrix elements ρ^J_{MM} by [27]

$$\rho^J_{MM} = \sum_K (-1)^{K-J-M} \langle J - MJM | K0 \rangle \rho_{KQ=0}, \quad (8)$$

where K and Q in relation (8) stand, respectively, for the rank of the tensor and its projection along the quantization axis. The relation (8) indicates that only the $Q=0$ components of the state multipoles are nonvanishing as the density matrix describing the atomic beam is diagonal in the photon frame. Using relations (6) and (8) the cross sections can be expressed in terms of irreducible tensor components as [15]

$$\frac{d^5\sigma}{d\Omega_f d\Omega_s dE_s} = \sum_{K=0}^{2J} \rho_{K0} \Lambda_0^{(K)}.$$
$$(9)$$

Expression (9) shows that the use of the state multipoles renders possible a separation of geometrical properties (de-

scribed by the state multipoles) and reaction dynamics (contained in the tensorial parameters $\Lambda_0^{(K)}$).

For low-energy scattering from a light target atom, such as sodium, one can neglect the relativistic interactions that might alter the spin projections of the continuum electrons without conservation of the total spin of the system. In this situation, the exchange process is the only spin-dependent process that needs to be taken into account. The spin part of the T-matrix elements appearing in relation (6) can then be factored out. In the present case of a sodium target, Eq. (9) can be expanded as [12,15]

$$\frac{d^5\sigma}{d\Omega_f d\Omega_s dE_s} = \frac{1}{3} \Lambda_0^{(0)} + \frac{1}{\sqrt{2}} (\rho_{11}^{(1)} - \rho_{-1-1}^{(1)}) \Lambda_0^{(1)}$$
$$+ \frac{1}{\sqrt{6}} (1 - 3\rho_{00}^{(1)}) \Lambda_0^{(2)}. \quad (10)$$

The tensorial components along the quantization axis of the target are expressed in terms of the state-resolved cross sections σ_{L,m_L} as

$$\Lambda_0^{(0)} = \frac{\kappa}{\sqrt{3}} (\sigma_{1,1} + \sigma_{1,0} + \sigma_{1,-1}), \quad (11)$$

$$\Lambda_0^{(1)} = \frac{\kappa}{\sqrt{2}} (\sigma_{1,1} - \sigma_{1,-1}), \quad (12)$$

$$\Lambda_0^{(2)} = \frac{\kappa}{\sqrt{6}} (\sigma_{1,1} - 2\sigma_{1,0} + \sigma_{1,-1}). \quad (13)$$

The cross sections σ_{L,m_L} are themselves expressed as functions of the symmetrized T-matrix elements as

$$\sigma_{L,m_l} = \kappa \sum_S \frac{1}{2S+1} |A\langle \mathbf{k}_f \nu_f \mathbf{k}_s \nu_s \Phi^{ion}_{L_i M_i} | T^S | \Phi^{atom}_{LM} \mathbf{k}_0 \nu_0 \rangle|^2.$$
$$(14)$$

These relations allow the calculation of the state-resolved cross section for arbitrary angles between the momentum transfer vector $\mathbf{q} = \mathbf{k}_0 - \mathbf{k}_f$ and the quantization axis $\mathbf{z}^{ph}$. In the experimental arrangement under consideration the atoms are prepared using circularly polarized light propagating perpendicular to the scattering plane [12]. In this situation the $\hat{\mathbf{z}}^{ph}$ quantization axis coincides with $\hat{\mathbf{z}}^n$, the quantization axis of the natural frame. As for the case of inelastic scattering studies [32], we define, for the present study, the natural frame as a right-handed coordinate system. In the natural frame, the quantization axis $\hat{\mathbf{z}}^{ph}$ is defined as $\hat{\mathbf{z}}^{ph} = \hat{\mathbf{k}}_0 \times \hat{\mathbf{k}}_f$.

The cross sections are calculated usually in the collision frame, where the quantization axis $\hat{\mathbf{z}}^c$ is defined along the incident electron momentum $\mathbf{k}_0$ and where, in coplanar kinematics, the fast electron is scattered in the (**xy**) plane. The collision and natural frames are related as

$$x^n = z^c, \quad y^n = x^c, \quad \text{and} \quad z^n = y^c. \quad (15)$$

The natural frame cross sections σ_{L,m_L} appearing in the expressions of the tensor components, Eqs. (11)–(13), can be expressed as functions of the collision frame scattering amplitudes by using the appropriate frame transformation through Euler angles [33,34]. The natural and collision frame scattering amplitudes, respectively $f^n_{m_L}$ and $f^c_{m_L}$, are related by

$$f^n_{\pm 1} = \mp \sqrt{\tfrac{1}{2}}[f^c_0 \pm \tfrac{1}{2}i(f^c_1 - f^c_{-1})], \qquad (16)$$

$$f^n_0 = -i\sqrt{\tfrac{1}{2}}(f^c_1 + f^c_{-1}). \qquad (17)$$

For the case of ionization, as for the case of inelastic scattering, reflection in the scattering plane also imposes the following relation for the collision frame scattering amplitudes:

$$f^c_1 = -f^c_{-1}. \qquad (18)$$

This reduces relations (16) and (17) to

$$f^n_{\pm 1} = \mp \sqrt{\tfrac{1}{2}}[f^c_0 \pm if^c_1], \qquad (19)$$

$$f^n_0 = 0. \qquad (20)$$

Using relations (18) and (19) in the expressions of the tensorial components (11)–(13), we see that the alignment parameter $\Lambda^{(2)}$ is related to the tensorial component $\Lambda^{(0)}$ as

$$\Lambda^{(2)}_0 = \sqrt{\tfrac{1}{2}}\Lambda^{(0)}. \qquad (21)$$

This indicates that in the present experimental arrangement the measurement of the initial-state averaged and state-selected cross sections allows determination of all three parameters describing the process, the scalar component $\Lambda^{(0)}$, which is the quantity usually measured in a conventional $(e,2e)$ experiment, and the vector component $\Lambda^{(1)}$, which is a measure of the change in the cross sections resulting from an inversion of the initial target orientation.

B. Scattering methods

To investigate the influence of the short- and long-range interactions, as well as the electron-electron interaction in the final state, we use two different scattering methods to evaluate the state-resolved cross sections. The first is the distorted-wave Born approximation (DWBA) [16,17], which accounts for the short- and long-range interactions in both the initial and the final states but treats the two outgoing electrons as independent particles. The second is the dynamically screened three-Coulomb-wave method (DS3C) [18], which accounts explicitly for the electron-electron correlation in the final state but in contrast neglects the short-range interaction in both the initial and final states.

In both approximations, the scattering from the Na atom is reduced to a three-body problem by considering only the active (valence) electron of the Na atom. The total Hamiltonian H of the projectile electron and target is

$$H = h_1 + h_2 + v_{12}, \qquad (22)$$

where h_1 and h_2 are the Hamiltonians of the active electrons, consisting of the kinetic energy operator K_i and potential V_i. v_{12} is the electron-electron interaction potential not included in V_i.

The DWBA approximation is formulated by partitioning the collision Hamiltonian into two parts [16,17],

$$H = (K_1 + U_1 + K_2 + V_2) + (V_1 + v_{12} - U_1), \qquad (23)$$

$$= K + V, \qquad (24)$$

where U_1 is the distorting potential, which needs to be defined [35]. When LS coupling is assumed to be valid for the $(N+1)$-electron state, the exact unsymmetrized T-matrix elements are approximated, within the DWBA, as

$$\langle \mathbf{k}_f \mathbf{k}_s \Phi^{\mathrm{ion}}_{J_i L_i M_i} | T | \Phi^{\mathrm{atom}}_{JLM} \mathbf{k}_0 \rangle$$
$$\equiv \langle \chi^{(-)}(\mathbf{k}_f) \chi^{(-)}(\mathbf{k}_s) | V | \phi_{LM} \chi^{(+)}(\mathbf{k}_0) \rangle. \qquad (25)$$

In relation (25), ϕ_{LM} is the one-electron orbital of the active target electron, the electron ejected from the atom during the ionization process. The distorted waves $\chi^{(\pm)}(\mathbf{k})$ are one-electron state solutions of the channel Hamiltonian K, separable in the electron coordinates. The DWBA T-matrix elements (25) can be derived by considering a post or prior form derivation [16,17]. In the former case, the entrance channel distorted wave $\chi^{(+)}(\mathbf{k}_0)$, which is the solution of the electron scattered by a central local potential U_1, approximates a formal distorted wave $X^{(+)}(\mathbf{k}_0)$ obtained by projecting the one-electron orbital ϕ_{LM} from an exact collision state $\Psi^{(+)}_\alpha(\mathbf{k}_0)$. In this situation, the distorted waves $\chi^{(\pm)}(\mathbf{k})$ are obtained by solving the elastic scattering problem in the field of the atom for the incoming and scattered electrons, $\chi^{(+)}(\mathbf{k}_0)$ and $\chi^{(-)}(\mathbf{k}_f)$, and in the field of the ion for the calculation of the distorted waves describing the scattering of the slow outgoing electron, $\chi^{(-)}(\mathbf{k}_s)$. In the prior formulation, the product of the two outgoing distorted waves $\chi^{(-)}(\mathbf{k}_f)$ and $\chi^{(-)}(\mathbf{k}_s)$, calculated in the field of the ion, approximates the exact collision state with final-state boundary condition $\Psi^{(-)}(\mathbf{k}_f,\mathbf{k}_s)$. In the next section we will use both of these formulations. We will refer to the post-form formulation as DWBAS and the prior-form formulation as DWBAI.

In both cases, the radial part of the distorted waves is derived as a solution of a radial equation of the type

$$\left(\frac{d^2}{dr^2} - \frac{l(l+1)}{r^2} - 2v(r) + k^2 \right) u_l(r) = 0. \qquad (26)$$

In Eq. (26), the potential $v(r)$ corresponds to the distorting potential $U_1(r)$ chosen as the equivalent local static-exchange potential of Furness and McCarthy [36] when scattering in the field of the atom is considered (e.g., for the incident and scattered electron distorted waves). The corresponding local static-exchange potential for the ion is chosen, in addition to the Coulomb potential, when the distorted waves are considered as electron-ion states.

We remark that in both alternatives of the DWBA the electron-electron interaction is not included in the calculation of the outgoing distorted waves. Thus, the bound-electron orbital and the distorted waves representing the slow escaping electron are orthogonal. Therefore, only the electron-electron interaction potential v_{12} contributes to Eq. (25).

In the second method considered here, the DS3C method, the exact T-matrix elements are approximated as

$$\langle \mathbf{k}_f \mathbf{k}_s \Phi_{J_i L_i M_i}^{\text{ion}} | T | \Phi_{JLM}^{\text{atom}} \mathbf{k}_0 \rangle \equiv \langle \Psi_f^{(-)}(\mathbf{k}_f, \mathbf{k}_s) | V | \phi_{L,M_L} \mathbf{k}_0 \rangle. \tag{27}$$

In relation (27), the initial state of the electron-atom system consists of the product of a plane wave describing the incoming projectile and a bound state describing the laser-excited atom state. The final state is reduced to a three-body system by assuming that the residual ion (Na^+) acts as a point charge on the two escaping electrons. The state of this three-body system is approximately represented by

$$\Psi_f^{(-)}(\mathbf{r}_f, \mathbf{r}_s) = N e^{i\mathbf{k}_f \cdot \mathbf{r}_f} e^{i\mathbf{k}_s \cdot \mathbf{r}_s} {}_1F_1[i\beta_f, 1, -i(k_f r_f + \mathbf{k}_f \cdot \mathbf{r}_f)]$$

$$\times {}_1F_1[i\beta_s, 1, -i(k_s r_s + \mathbf{k}_s \cdot \mathbf{r}_s)]$$

$$\times {}_1F_1[i\beta_{fs}, 1, -i(k_{fs} r_{fs} + \mathbf{k}_{fs} \cdot \mathbf{r}_{fs})], \tag{28}$$

where $\mathbf{r}_{fs} = \mathbf{r}_f - \mathbf{r}_s$ and $\mathbf{k}_{fs} = (\mathbf{k}_f - \mathbf{k}_s)/2$. ${}_1F_1[a,b,c]$ is the confluent hypergeometric function while N is a normalization factor. The form of the dynamical Sommerfeld parameters β_i can be found in [18,37]. The interpretation of the wave function (28) is straightforward. It assumes that the three-body system consists of three two-body subsystems. The interaction strength within each individual subsystem is dictated by the coupling to the other remaining two-body subsystems. This coupling is contained in the Sommerfeld parameters. The final-state wave function within the first Born approximation is readily obtained from Eq. (28) upon the replacement $\beta_f \equiv 0 \equiv \beta_{fs}$, $\beta_s = -Z_{\text{Na}^+}/k_s$, where Z_{Na^+} is the charge of the residual ion. If we consider the two final-state electrons to be moving independently in the field of Na^+, the Sommerfeld parameters in the wave function (28) reduce to $\beta_s = -Z_{\text{Na}^+}/k_s$, $\beta_f = -Z_{\text{Na}^+}/k_f$, $\beta_{fs} \equiv 0$.

IV. RESULTS AND DISCUSSION

To establish the validity of the two scattering methods presented in the previous section for the particular kinematics considered here, we first concentrate on the description of the ionization process of ground-state sodium atoms. In Fig. 5, we present DWBA calculations for the ionization of $^2S_{1/2}$ ground-state sodium for four different kinematical arrangements.

Within the DWBA method, a Slater representation of the sodium Hartree-Fock orbitals, as tabulated by Clementi and Roetti [38], is used for the target radial orbitals. This representation is used to generate the bound-electron radial orbital as well as the static potential in the calculation of the distorted waves. As mentioned earlier, the equivalent spin-average local exchange potential of Furness and McCarthy [36] is used to generate the exchange part of the distorting

potential in both the entrance and exit channels. It is noted here that the DWBA calculations presented in this paper have not been energy averaged over the 6 eV energy band over which scattered electrons are detected, but rather calculated at the mean value of this energy band for each of the two analyzers separately.

Figure 5 shows DWBA calculations for the two different derivations of the DWBA T-matrix elements presented in the previous section compared to measurement. The dashed line corresponds to the post-form derivation, where both the incident and scattered distorted waves are calculated in the distorting potential U_1, and the solid line to the prior-form derivation where both outgoing electrons are calculated as electron-ion states. Since the measurements are not absolute, the only valid comparison of theory with experiment is one of shape. Having chosen the form of the DWBA, normalization of the data to theory is via the $3p$ cross section as discussed later. This gives the ground-state normalization factors indicated in the caption of Fig. 5. Shape comparison with the experimental measurements indicates that the prior-form derivation provides a better description of the ionization process of the ground-state sodium atom for all the kinematics considered here. The post-form formulation results in a cross section where the maximum is slightly shifted toward lower values of the slow electron angle. This shift of the maximum of the cross sections toward smaller values of the slow electron angle increases in the DWBAS calculation as the incident energy decreases. For the lowest value of the incident electron energy considered here, $E_0 = 60$ eV, the binary peak of the cross sections when calculated using the DWBAS formulation is shifted to lower values of the slow electron angle by almost 20° when compared to both the DWBAI calculation and the experimental measurements. In terms of the magnitudes of the ionization cross section, while the DWBAS and DWBAI calculations predict values of almost identical magnitude for the incident energy $E_0 = 151$ eV, the DWBAI formulation predicts smaller magnitudes for the cross sections as the incident energy decreases. However, since the measurements (a) to (d) have not been cross-normalized experimentally, the energy dependence of the two calculations cannot be directly compared against that of experiment.

Normalization of experiment to theory has been performed in the following manner. The excited-state experimental $3p$ cross sections, which form the main focus of this paper, are normalized to the DWBAI theory based on its superior description of the shapes of the ground-state cross sections. Given that the $3s/3p$ cross-section ratios are determined experimentally for each kinematics, within an error of 20% [see Eqs. (2) and (3)], multiplicative coefficients are applied to the ground-state theoretical calculations shown in Fig. 5 for best comparison with the shape of the experimental cross sections. The coefficients for the DWBAI calculations reflect how the $3S/3P$ cross-section ratio, as predicted within the DWBAI model, compares to that derived from experiment. The values of these coefficients, which vary from 1.32 at 151 eV to 2.15 at the lowest energy, clearly indicate that the branching ratio is underestimated for three of the kinematic regimes considered here [graphs (a), (b), and (d)]. A
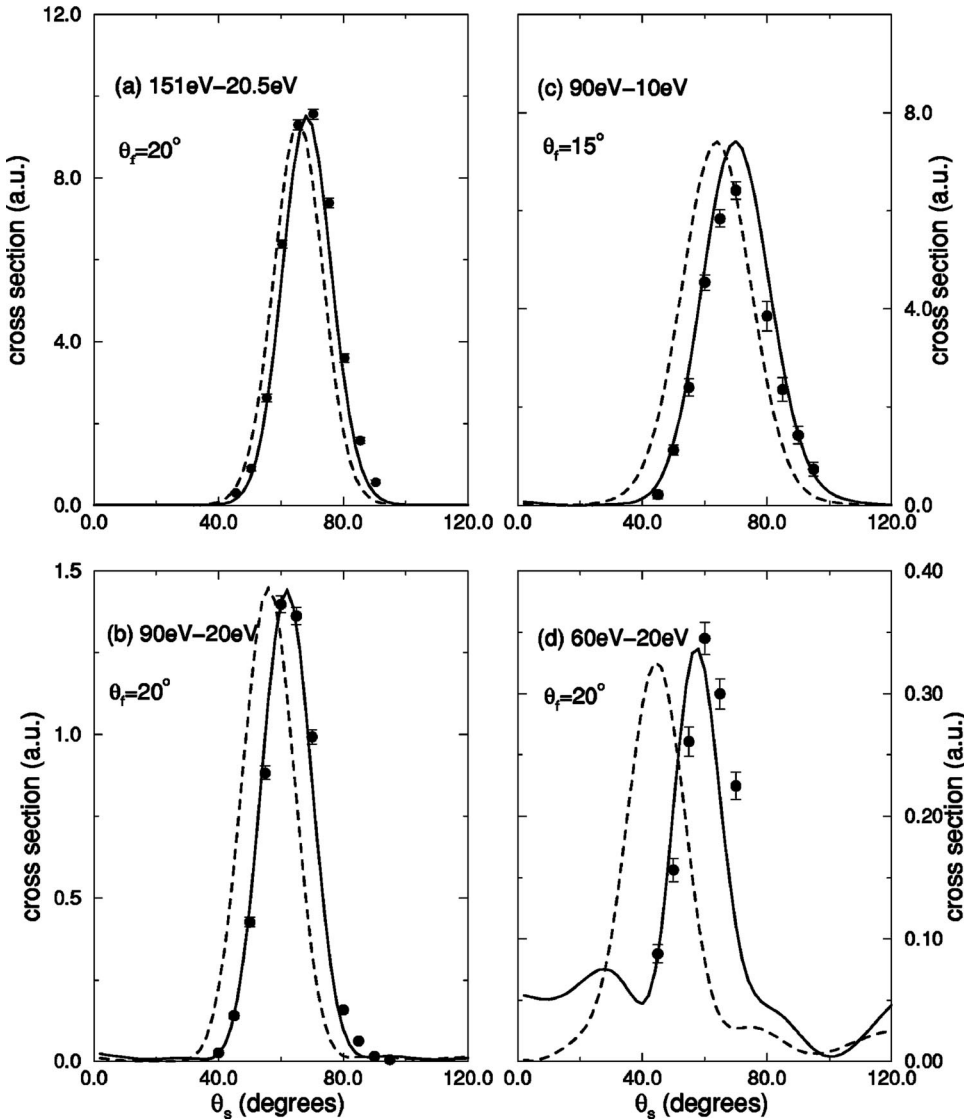
FIG. 5. Variation of the cross sections as a function of the slow electron angle for the ionization of ground-state sodium. DWBAI (solid line), DWBAS (dashed line). (a) $E_0 = 151$ eV, $E_s = 20.5$ eV, and $\theta_f = 20°$; (b) $E_0 = 90$ eV, $E_s = 20$ eV, and $\theta_f = 20°$; (c) $E_0 = 90$ eV, $E_s = 10$ eV, and $\theta_f = 15°$; and (d) $E_0 = 60$ eV, $E_s = 20$ eV, and $\theta_f = 20°$. The DWBAI calculations are multiplied by 1.32 (a), 1.46 (b), 1 (c), and 2.15 (d). The DWBAS calculations are multiplied by 1.2 (a), 1.1 (b), 0.78 (c), and 1.2 (d). The data are normalized to the DWBAS excited-state cross sections as discussed in the text.

coefficient of 1.0 is applied to the DWBAI calculations shown on graph (c), indicating that in this case the ratio of the $3S/3P$ cross section now appears to be slightly overestimated.

Nevertheless, the figure does show that the prior-form formulation is superior in describing quantitatively the angular behavior of the experimental data over the whole kinematical range considered here. The comparison between prior-form results and experimental measurements suggests that approximating the exact final-state wave function $\Psi^{(-)}(\mathbf{k}_f, \mathbf{k}_s)$ as the product of two Coulomb waves gives a reasonable description of the position of the binary peak of the cross sections over the range of kinematics considered here.

We now turn to the main focus of the present study, description of the ionization of laser-excited $3P$ sodium atoms. In the DWBA calculations, the excited sodium atoms are also described using a Slater representation of the Hartree-Fock orbitals. The Hartree-Fock orbitals are in this case generated using the Hartree-Fock program of Fischer [39]. For the DS3C calculations, a Klapisch-type potential is used to generate the excited bound electron orbital [40,41].

The thick solid and dashed curves of Fig. 6 shows the state-resolved cross sections $\sigma_{1,1}$ and $\sigma_{1,-1}$, when calculated using the prior form of the DWBA method. The experimental measurements have not been normalized to one another and hence are individually normalized to the excited-state DWBAI theory for each of the kinematics considered, as discussed earlier. The figure shows that the DWBAI model is reasonably successful in predicting the correct relative magnitude of the state-resolved cross sections at each of the kinematics presented. The most obvious discrepancy is at the incident energy of 151 eV, where the theoretical prediction indicates that the state-resolved cross sections are of almost the same magnitude while the experimental cross sections, in contrast, show the $\sigma_{1,1}$ cross section to be significantly smaller than the $\sigma_{1,-1}$ cross section. The double-peak structure in the $\sigma_{1,1}$ cross section is also not reproduced in the calculation. Recently, it has been argued [42] that the origin of this structure lies in the final-state interaction of the slow electron with the residual ion. However, the scattering geometry investigated was slightly different from the present case.

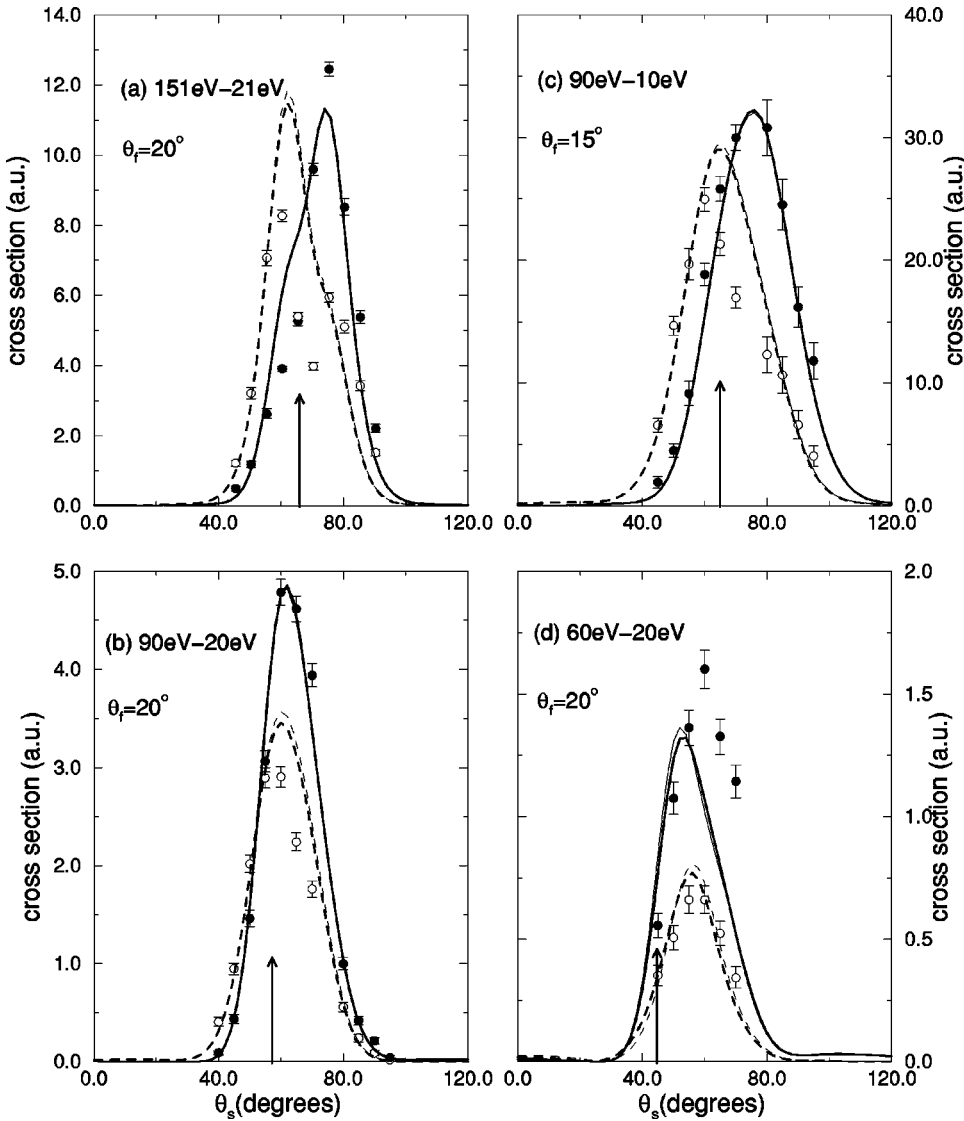For the lower value of the incident electron energy, E_0

FIG. 6. Variation of the cross sections as a function of slow electron angle for the ionization of $3P$ excited sodium. Filled circles, measured $\sigma_{1,-1}$ (Na $3^2P_{3/2}$, $m_F = -3$); open circles, $\sigma_{1,1}$ ($m_f = +3$). DWBAI calculations $\sigma_{1,-1}$ (thick solid line) and $\sigma_{1,1}$ (thick dashed line) and DWBACF calculations $\sigma_{1,-1}$ (thin solid line) and $\sigma_{1,1}$ (thin dashed line). See text for details. The experimental measurements are normalized to the maximum of the DWBA $\sigma_{1,-1}$ calculations for (a)–(c) and to the maximum of DWBA $\sigma_{1,1}$ for (d). The kinematics are as in Fig. 5. The arrow indicates the direction of the momentum transfer **q**.

$= 90$ eV, the relative magnitudes of the experimental cross sections $\sigma_{1,-1}$ and $\sigma_{1,1}$ are also clearly different. In this case, for a slow electron ejected at an energy E_s of either 10 or 20 eV and at a scattering angle θ_f of 15° and 20°, respectively, the magnitude of $\sigma_{1,1}$ is consistently smaller than $\sigma_{1,-1}$. As can be seen from Fig. 6, the relative magnitudes of the state-resolved cross sections are predicted reasonably well by the DWBA method; however the ratio of peak heights is underestimated by the theoretical model while the experimental measurements of $\sigma_{1,1}$ suggest a slightly narrower binary peak for both kinematics. Further, a mild shoulder evident in the experimental $\sigma_{1,1}$ is not reproduced by the theory when the slow electron is ejected with an energy of $E_s = 10$ eV. At $E_0 = 60$ eV, the relative magnitude of $\sigma_{1,-1}$ and $\sigma_{1,1}$ is still reasonably well described by the DWBA model although again underestimated. However, the theoretical prediction for the position and relative height of the binary peak in $\sigma_{1,-1}$ is now at variance with the experimental data, its angle being shifted by around 5° toward lower angles.

To further investigate the mechanism responsible for this breaking of symmetry around the momentum transfer direc-

tion we used two additional models to calculate the state-resolved cross sections. In the first model, DWBAPF, the scattered electron is described by a plane wave while the incident and ejected electron are described using the same distorting potential as described in the previous section. In the second model, DWBACF, the distorting potential used to calculate the fast-electron distorted wave is replaced by the Coulomb potential only.

The DWBACF calculations are represented by the thin solid and dashed curves in Fig. 6. Comparison between the DWBA and DWBACF calculations in this figure indicates that, for the kinematics considered in this study, the short-range interactions, static and exchange, between the scattered electron and the remaining electrons of the ion have a minimal influence on the position of the maximum of the cross sections or on the relative magnitudes of the state-resolved cross sections. We note in the figure that the $\sigma_{1,1}$ cross sections calculated within the DWBACF are normalized to the corresponding DWBA calculations for each kinematics. Nonetheless, we can see that the short-range interactions tend to increase the difference in magnitude between $\sigma_{1,1}$
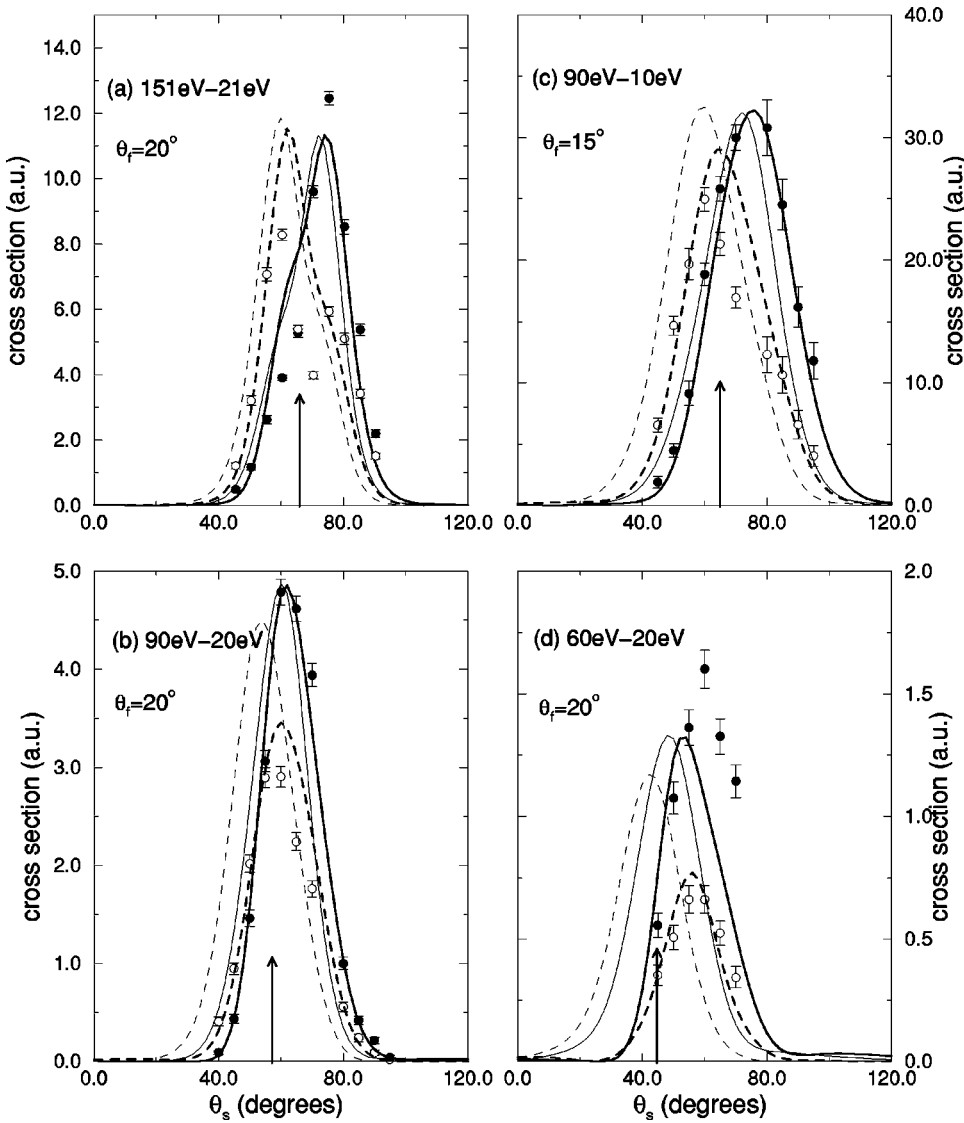
FIG. 7. Influence of the Coulomb interaction for the scattered electron on the variation of the cross sections as a function of the slow electron angle for the ionization of $3P$ sodium. Same legend details as in Fig. 6; the DWBAI calculations are shown as thick lines, the DWBAPF calculations as thin lines. The DWBAPF calculations are multiplied by 0.87 (a), 0.80 (b), 0.83 (c), and 0.75 (d). Same kinematics as in Fig. 5.

and $\sigma_{1,-1}$ by the same amount for all cases.

In contrast, the comparison between the DWBAPF and DWBA calculations, shown in Fig. 7, indicates an increasingly strong influence of the Coulomb interaction of the scattered electron with the residual ion when the incident electron energy decreases. This is comprehensible, as the dichroism as such vanishes when all interactions of the ejected electrons with the ion are neglected. At lower energies the interactions of both electrons with the residual ion become of the same order and hence we can expect the dichroism to be influenced by both of these interactions.

For an incident electron energy of 151.6 eV and at the kinematical arrangement of the present experiment, theory suggests that the Coulomb interaction between the scattered electron and the residual ion has a minor effect on the shape and magnitude of the dichroism. This situation changes drastically when the incident energy is lowered to 90 eV. As deduced from Fig. 7 the Coulomb interaction of the fast electron with the ion is largely responsible for the break in reflection symmetry of the state-resolved cross sections with respect to $\hat{\mathbf{q}}$. Furthermore, the positions of the binary peaks

in both of the state-resolved cross sections are shifted toward larger ejection angles. The dichroism is then correspondingly modified. At the moment it is not clear why this shift proceeds in that direction when the final-state interaction of the projectile electron is taken into account.

At yet lower energies ($E_0 = 60$ eV), the situation becomes more delicate. Obviously the magnitude of the dichroism is underestimated by the DWBA calculations (cf. Fig. 7). Nevertheless, the DWBA model predicts a shift of the binary peak positions with respect to the momentum transfer direction in the direction shown by the experiments. Again this shift can be associated with the Coulomb final-state interaction of the scattered electron with the residual ion (cf. Fig. 8).

In earlier work [12] we suggested that the electron-electron final-state interaction, missing in the DWBA, becomes important at this low energy. This conjecture is tested by the DS3C calculations shown in Fig. 8(d) in which we systematically switch on the various final-state interactions and explore their influence.

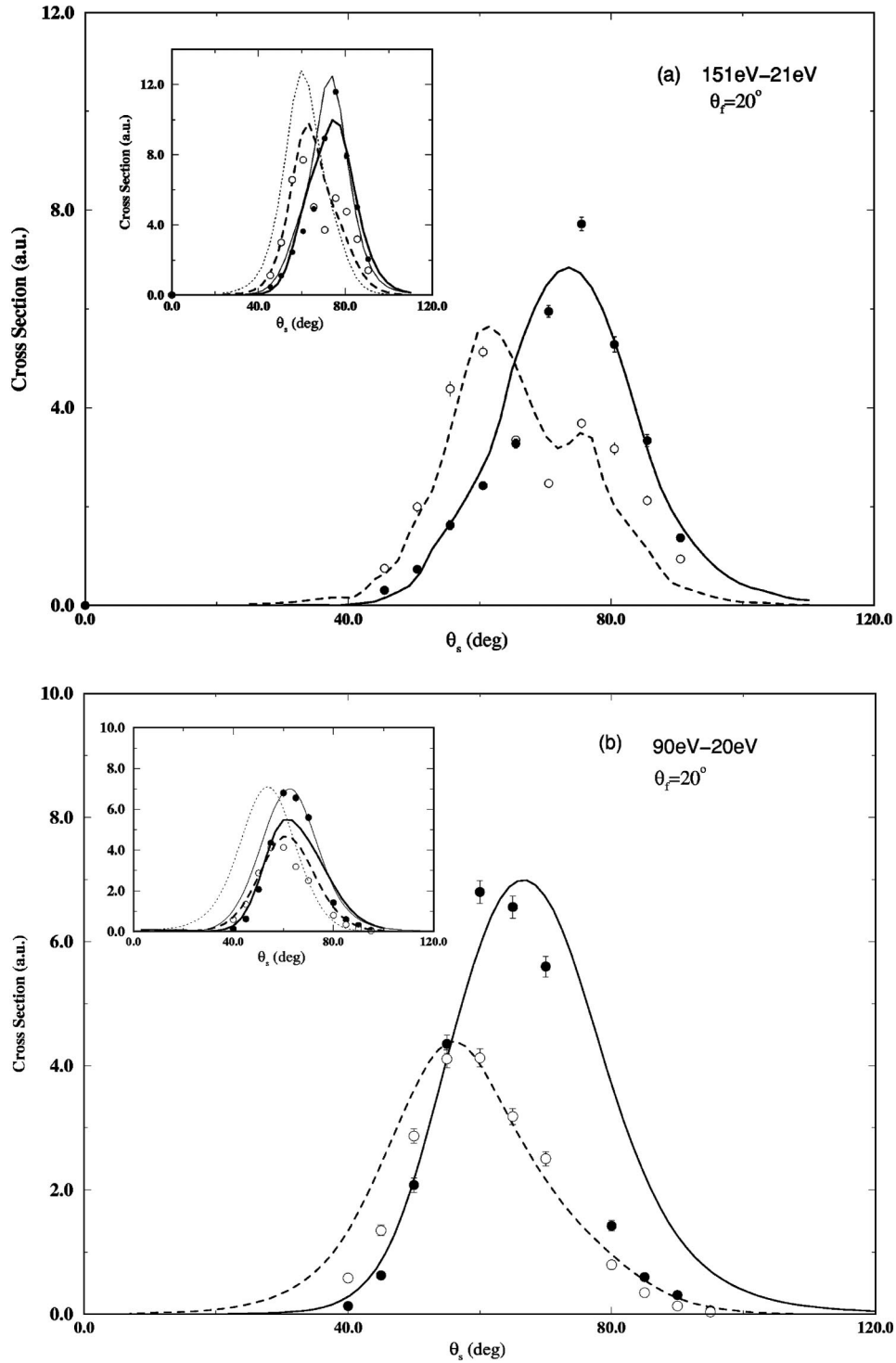For all DS3C calculations presented in this work an aver-

FIG. 8. The same kinematical arrangement as in Fig. 5. In (a) the incident energy is $E_0 = 151.62$ eV, the median energy of the ejected electron is $E_s = 21.5$ eV (additional 1.0 eV energy due to weaker binding energy of $3p$ electron), and the scattered electron angle is $\theta_s = 20°$. The calculations for $\sigma_{1,-1}$ (solid curve) and $\sigma_{1,1}$ (dashed curve) are performed within the DS3C model including exchange. An average has been performed over the 6 eV range of energies over which the outgoing electrons are detected in all the calculations at all the kinematics. For best shape comparison, the experimental results have been normalized to the DS3C theory. The inset shows the FBA results (light solid curve for $\sigma_{1,-1}$ and light dashed curve for $\sigma_{1,1}$) and the results (solid curve represents $\sigma_{1,-1}$ and dashed curve is $\sigma_{1,1}$) when the two escaping electrons move independently in the field of the residual ion, i.e., we set in Eq. (28) $\beta_{fs} \equiv 0$, $\beta_s = -Z_{Na^+}/k_s$, $\beta_f = -Z_{Na^+}/k_f$. For inset in (a) only the experimental results, after normalization to the DS3C theory, have been multiplied by an additional factor of 1.5 to facilitate comparison with the FBA calculations. In (b) the same labeling of curves as in (a) but the incident energy is lowered to $E_0 = 90$ eV. In (c) the same as in (b) but the scattering angle is fixed to $\theta_f = 15°$ and the ejected electron energy is chosen as $E_s = 10$ eV. The FBA calculations are not shown in the inset. (d) the 60 eV data with the same descriptions of curves.
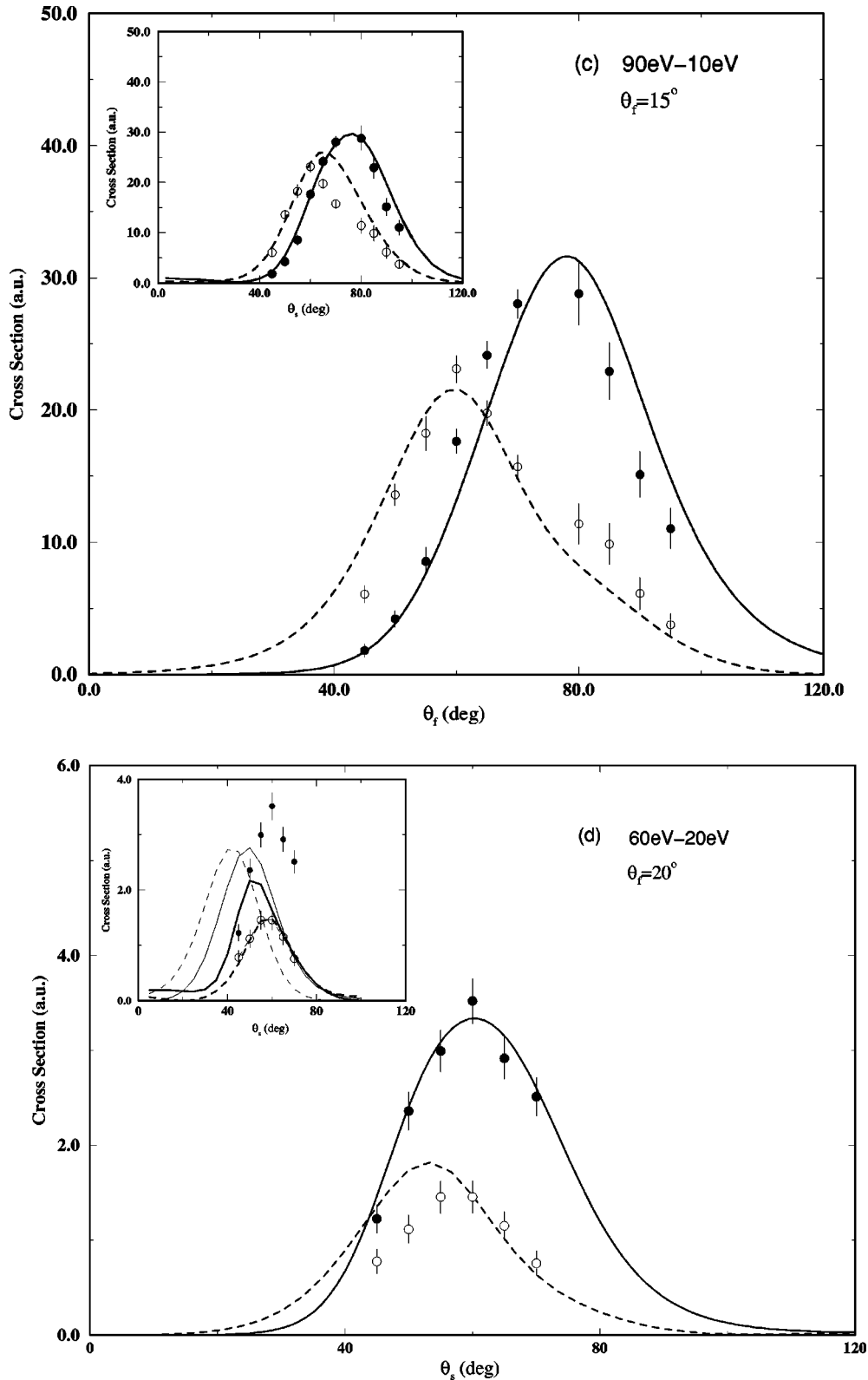
FIG. 8 (*Continued*).

age has been performed over the 6 eV range of energies over which outgoing electrons are detected. For best shape comparison, the experimental results have been normalized to the DS3C theory. If all final-state interactions are neglected $[\beta_f \equiv \beta_s \equiv \beta_{fs} \equiv 0$ in Eq. (28)] the dichroism vanishes. Upon

replacing in Eq. (28) $\beta_f \equiv 0 \equiv \beta_{fs}$, $\beta_s = -Z_{Na^+}/k_s$ (the FBA case) we obtain a finite dichroism with the symmetry properties mentioned above. If we set in Eq. (28) $\beta_{fs} \equiv 0$, $\beta_s = -Z_{Na^+}/k_s$, $\beta_f = -Z_{Na^+}/k_f$ (independent Coulomb particles) the binary peaks in the cross sections are shifted toward

larger ejection angles, as in the case of Fig. 7. Now taking the electron-electron final-state interactions into account results in a further shift of the binary peaks and an increase in the dichroism. The direction of the shift, however, is not simply one to larger angles as would be expected on the basis of mutual repulsion of the two escaping electrons. Figure 8(d) shows the direction and magnitude of the shift to depend upon the initial magnetic quantum state of the bound electron state. This implies a dynamical role of the electron-electron interaction beyond a simple repulsion effect. In particular, the ionization via direct scattering from the core is greatly enhanced when the interelectronic correlation is taken into account. This is because, in the FBA and within a frozen core approximation, ionization following direct scattering from the nucleus is not allowed due to the orthogonality of initial and final target states. This situation is not altered when the interaction of the scattered electron with the residual ion is taken into account, since the two escaping electrons are still decoupled. It is the coupling between these two electrons that makes possible an ionization event after a direct projectile-core scattering. At yet lower energies, more drastic effects of the electron-electron interaction have been anticipated [15]. All DS3C calculations shown in Fig. 8 are energy averaged over the 6 eV range over which the outgoing electrons are detected.

For the higher-incident-energy cases [Figs. 8(a)–8(c)] the effect of the electron-electron final-state interaction on the *shape* of the cross sections becomes less pronounced under the kinematics of concern here, which are primarily dictated by the final-state interactions of the escaping electrons with the residual ion. This in accord with the conclusions of the DWBA calculations. From the results depicted in Fig. 7 and Figs. 8(a)–8(d) we can conclude, however, that the absolute *values* of the cross sections are considerably affected by the interelectronic final-state interaction. This is in line with recent conclusions for the electron-impact ionization of isotropic targets [43]. It is interesting to note that the double peak in the $\sigma_{1,1}$ cross section for the 151 eV kinematics [Fig. 8(a)] is reproduced in the DS3C calculations.

V. CONCLUSIONS

In this work we have presented fully differential cross sections for the electron-impact ionization of the sodium atom laser pumped into a selected magnetic sublevel. It is demonstrated, experimentally and theoretically, that the spectra of the emitted electrons depend in a nontrivial manner on the helicity of the absorbed photon. For the asymmetric kinematics considered in this work, our findings can be summarized as follows. At an intermediate incident energy of 151.6 eV and for the scattered angles presented here, theory suggests that the dichroism and the individual cross sections are essentially determined by the interactions of the slow outgoing electron with the residual ion, whereas the interelectronic coupling as well as the interaction of the fast outgoing electron with the residual ion play a minor role. However, discrepancies between theory and experiment still exist under these conditions, precluding definitive statements on the nature of the dichroism. At yet lower energies, 90 eV, the scattering dynamics, and hence the cross sections, become sensitive to the interaction of the fast outgoing electron with the residual ion while the final-state electron-electron correlation is of less importance. This situation is reflected in increasing deviations from reflection symmetry (with respect to the momentum transfer direction) of the state-resolved cross section. The strong symmetry breaking is confirmed by experimental measurements. At the lowest incident energy considered here (60 eV), the cross sections become sensitive to all interactions, and, in particular, the final-state electron-electron interaction needs to be taken into account. These conclusions are substantiated by the experimental findings. As a result of the present study, it is anticipated that even at higher incident energy, the inclusion of the electron-electron interaction will prove indispensible for certain kinematical situations where the two electrons are close to each other in velocity space or when a strong scattering from the nucleus is unavoidable, e.g., in backscattering geometry.

[1] I. E. McCarthy and E. Weigold, Phys. Rep., Phys. Lett. **27C**, 275 (1976).

[2] I. E. McCarthy and E. Weigold, Rep. Prog. Phys. **54**, 789 (1991).

[3] G. Baum, W. Blask, P. Freienstein, L. Frost, S. Hesse, W. Rith, P. Rappolt, and M. Streun, Phys. Rev. Lett. **69**, 3037 (1992).

[4] H. Th. Prinz, K. H. Besch, and W. Nakel, Phys. Rev. Lett. **74**, 243 (1995).

[5] X. Guo, J. Hurn, J. Lower, S. Mazevet, Y. Shen, E. Weigold, B. Granitza, and I. E. McCarthy, Phys. Rev. Lett. **76**, 1228 (1996).

[6] A. Dorn, A. Elliot, X. Guo, J. Hurn, J. Lower, S. Mazevet, I. E. McCarthy, Y. Shen, and E. Weigold, J. Phys. B **30**, 4097 (1997).

[7] S. Keller, C. T. Whelan, H. Ast, H. R. J. Walters, and R. M. Dreizler, Phys. Rev. A **50**, 3865 (1994).

[8] G. F. Hanne, in *Proceedings of the Seventeenth International Conference on the Physics of Electronic and Atomic Collisions*, edited by W. R. MacGillivray, I. E. McCarthy, and M. C. Standage (IOP Publishing, Ltd., Bristol, 1991), p. 199.

[9] D. H. Madison, V. D. Kravtsov, and S. Mazevet, J. Phys. B **31**, L17 (1998).

[10] D. H. Madison, V. D. Kravtsov, S. Jones, and R. P.

McEachran, Phys. Rev. A **53**, 2399 (1996).

[11] M. Fehr, J. Berakdar, and H. Klar, J. Phys. B **27**, L401 (1994).

[12] A. Dorn, A. Elliot, J. Lower, E. Weigold, J. Berakdar, A. Engelns, and H. Klar, Phys. Rev. Lett. **80**, 257 (1998).

[13] J. Berakdar, A. Dorn, A. Elliot, J. Lower, and E. Weigold, J. Electron Spectrosc. Relat. Phenom. **88-91**, 50 (1998).

[14] J. Berakdar, A. Dorn, A. Elliot, J. Lower, and E. Weigold, in *Proceedings of the Twentieth International Conference on the Physics of Electronic and Atomic Collisions*, edited by F. Aumayr and H. Winter (World Scientific, Singapore, 1998), p. 295.

[15] J. Berakdar, A. Engelns, and H. Klar, J. Phys. B **29**, 1109 (1996).

[16] I. E. McCarthy and E. Weigold, *Electron-Atom Collisions* (Cambridge University Press, Cambridge, England, 1995).

[17] I. E. McCarthy, Aust. J. Phys. **48**, 1 (1995).

[18] J. Berakdar, Phys. Rev. A **53**, 2314 (1996).

[19] A. Dorn, A. Elliott, J. Lower, S. F. Mazevet, R. P. McEachran, I. E. McCarthy, and E. Weigold, J. Phys. B **31**, 547 (1998).

[20] D. T. Pierce, R. J. Celotta, G. C. Wang, W. N. Unertl, A. Galejs, C. E. Kuyatt, and S. R. Mielczarek, Rev. Sci. Instrum. **51**, 478 (1980).

[21] S. D. Kevan, Rev. Sci. Instrum. **54**, 1441 (1983).

[22] J. J. McClelland, M. H. Kelly, and R. J. Celotta, Phys. Rev. A **40**, 2321 (1989).

[23] J. F. Kelly and A. Gallagher, Rev. Sci. Instrum. **58**, 563 (1987).

[24] E. E. B. Campbell, H. Hulser, R. Witte, and I. V. Hertel, J. Phys. D **16**, 21 (1990).

[25] J. Lower and E. Weigold, J. Phys. E **22**, 421 (1989).

[26] K. Bartschat, Phys. Rep. **180**, 1 (1988).

[27] K. Blum, *Density Matrix Theory and Applications* (Plenum, New York, 1981).

[28] J. Kessler, *Polarised Electrons*, 2nd ed. (Springer-Verlag, Berlin, 1985).

[29] S. Mazevet, I. E. McCarthy, and E. Weigold, Phys. Rev. A **57**, 1881 (1998).

[30] I. Percival and M. J. Seaton, Philos. Trans. R. Soc. London, Ser. A **251**, 113 (1958).

[31] A. Fisher and I. V. Hertel, Z. Phys. A **304**, 103 (1981).

[32] I. V. Hertel, M. H. Kelley, and J. J. McClelland, Z. Phys. D: At., Mol. Clusters **6**, 163 (1987).

[33] N. Andersen, I. V. Hertel, and K. Kleinpoppen, J. Phys. B **17**, L901 (1984).

[34] D. M. Brink and G. R. Satchler, *Angular Momentum*, 2nd ed. (Clarendon Press, Oxford, 1968).

[35] H. Klar, D. A. Konovalov, and I. E. McCarthy, J. Phys. B **19**, 1803 (1986).

[36] J. B. Furness and I. E. McCarthy, J. Phys. B **6**, 2280 (1973).

[37] J. Berakdar, J. S. Briggs, I. Bray, and D. V. Fursa, J. Phys. B **32**, 895 (1999).

[38] E. Clementi and C. Roetti, At. Data Nucl. Data Tables **14**, 177 (1974).

[39] C. F. Fischer, Comput. Phys. Commun. **43**, 355 (1987).

[40] M. Klapisch, Ph.D. thesis, University of Paris–sud, Orsay, 1969 (unpublished).

[41] M. Klapisch, M. Machholm, and E. Lawartowski, Z. Phys. D: At., Mol. Clusters **30**, 205 (1994).

[42] J. Berakdar and S. Mazevet, J. Phys. B **32**, 9365 (1999).

[43] J. Berakdar, Phys. Rev. A **56**, 370 (1997).